

1 **Apparent directional mass-transfer capacity**
2 **coefficients in three-dimensional anisotropic**
3 **heterogeneous aquifers under radial convergent**
4 **transport**

D Pedretti, Department of Earth, Ocean and Atmospheric Sciences, University of British Columbia, 2207 Main Mall, V6T1Z4, Vancouver BC, Canada (email: dpedretti@eos.ubc.ca).

D Fernandez-Garcia, X Sanchez-Vila, Hydrogeology Group, Department of Geotechnical Engineering and Geo-Sciences, UPC-Barcelona Tech, Spain.

D Bolster, Department of Civil and Environmental Engineering and Earth Sciences, University of Notre Dame, USA.

D A Benson, Hydrologic Science and Engineering, Colorado School of Mines, Golden CO USA.

5 **Abstract.** Aquifer hydraulic properties such as hydraulic conductivity
6 (K) are ubiquitously heterogeneous and typically only a statistical charac-
7 terization can be sought. Additionally statistical anisotropy at typical char-
8 acterization scales is the rule. Thus, regardless of the processes governing so-
9 lute transport at the local (pore) scale, transport becomes non-Fickian. Mass-
10 transfer models provide an efficient tool that reproduces observed anoma-
11 lous transport; in some cases though, these models lack predictability as model
12 parameters cannot readily be connected to the physical properties of aquifers.
13 In this study we focus on a multi-rate mass-transfer model (MRMT), and
14 in particular the apparent capacity coefficient (β), which is a strong indica-
15 tor of the potential of immobile zones to capture moving solute. We aim to
16 find if the choice of an apparent β can be phenomenologically related to mea-
17 sures of statistical anisotropy. We analyzed an ensemble of random simula-
18 tions of three-dimensional log-transformed multi-Gaussian permeability fields
19 with stationary anisotropic correlation under convergent flow conditions. It
20 was found that apparent β also displays an anisotropic behavior, physically
21 controlled by the aquifer directional connectivity, which in turn is controlled
22 by the anisotropic correlation model. A high hydraulic connectivity results
23 in large β values. These results provide new insights into the practical use
24 of mass-transfer models for predictive purposes.

1. Introduction

25 Anisotropy and heterogeneity of hydraulic properties such as the hydraulic conductivity
26 (K) are intrinsic to aquifers worldwide (e.g., [Rubin, 2003]). Both features are linked to
27 the geologic origin of aquifers and are not easily characterizable at the scales where solute
28 transport typically occurs. A lack of detailed knowledge of the spatial distribution of
29 hydraulic parameters at the local scale gives rise to uncertain spatio-temporal distributions
30 of solute plumes, which has significant consequences for the prevention of groundwater
31 pollution as well as the management and remediation of polluted aquifers (e.g., [Bolster
32 *et al.*, 2009; de Barros *et al.*, 2011])

33 Macroscopic anisotropy is a very well-known phenomenon in structural geology related
34 to sedimentological processes, faulting and folding, and metamorphic processes. While in
35 hydrogeology it is common to refer to anisotropic formations as vertically axisymmetric
36 media (e.g., stratified formations such as those present at the Grand Canyon, Colorado
37 River, USA, depicted at the bottom of Fig. 1), other forms of anisotropic formations also
38 exist, such as those shown on the top of Fig. 1. Fig. 1-A depicts a conceptual sketch
39 by *Koltermann and Gorelick* [1996] of oriented coarse-grained deposits embedded in a
40 fine-grained matrix. The origin of these deposits is fluvial; well-connected coarse-grained
41 structures appear to be distributed along one principle direction. Fig. 1-(B) corresponds
42 to an outcrop of vertically-oriented planes of fractures in a gneiss formation in Cordoba
43 (Spain). The fractures originated from recent tectonic activities, and their orientation is
44 collinear with the main stratification of the rock formation, tilted by an angle of 80-85
45 degrees (i.e., subvertical). In this case, preferential flow paths along quasi-vertical planes

46 are expected. It should be noted that the observation of anisotropy is scale-dependent.
47 An anisotropic description at the field scale gives no information as to whether or not the
48 local behavior is isotropic.

49 Because it is infeasible to exhaustively model all local scale heterogeneous patterns af-
50 fecting flow and solute transport dynamics, alternative (*effective*) models are powerful
51 tools for capturing pertinent dynamics. These models aim to reproduce the average be-
52 havior of flow and solute plumes by means of upscaled (averaged) mathematical operators
53 (such as macrodispersive terms) or using alternative mathematical models (such as nonlo-
54 cal formulations) (e.g., [Rubin, 2003]). In the context of (statistically) anisotropic porous
55 media, effective models have been studied extensively since the early work on flow in per-
56 fectly stratified formations by Gelhar *et al.* [1979]. These authors were the first to derive
57 values of directional effective K in randomly heterogeneous media. Later, many others
58 developed a suite of solutions for expected values and uncertainties (variances) for flow
59 and solute concentrations in statistically anisotropic media under uniform flow conditions
60 (see e.g. [Rubin, 2003]).

61 Significantly less work focuses on flow and transport under convergent (radial) flow
62 conditions. Sanchez-Vila and Carrera [1997] showed that convergent flow tracer tests
63 (CFTTs) in statistically non-isotropic media leads to variable directional travel times,
64 which resulted in the concept of *apparent directional advective porosities*. It is impor-
65 tant to note that CFTTs are sometimes preferable to uniform flow tracer tests in field
66 applications for economic reasons (e.g., [Ptak *et al.*, 2004]); additionally the analysis of
67 convergent forced-gradient flow and solute transport problems is relevant in several prac-

68 tical circumstances such as delineation of well-capture zones or aquifer remediation using
69 pump-and-treat activities.

70 Much previous work on upscaled transport in heterogeneous media departs from the
71 assumption that conservative solutes in the subsurface can be perfectly modeled with an
72 advection-dispersion equation (ADE). In recent years, this approach has been criticized
73 due to its poor ability to properly reproduce field observations; observed BTCs from
74 field experiments often display early arrivals, greater concentrations in late-time tails
75 and highly nonsymmetric (skewed) distributions, while BTCs predicted by the ADE are
76 generally symmetric (non skewed). Non-symmetric distributions of BTCs are also typi-
77 cally referred to as having *tailing*, and all these discrepancies between field observation
78 and ADE predictions are lumped together under the general term *anomalous transport*.
79 Among several causes that can explain the failure of the ADE, we highlight here the lim-
80 ited resolution and dimensionality of numerical models using the ADE, the assumption
81 of multi-Gaussianity for $\ln K$ multivariate distributions, the lack of consideration of flow
82 distributions other from uniform, and the assumption of ergodicity.

83 The dimensionality issue can be exemplified by the limited ability of two-dimensional
84 (2D) ADE-based numerical simulations to reproduce anomalous transport. 2D numerical
85 setups are largely adopted for practical reasons due to the lower computational burden
86 compared with 3D simulations. However, when used to simulate transport using the
87 ADE model (especially assuming unconditional multi-Gaussian K fields), 2D models offer
88 a limited capacity to reproduce observed anomalous transport, leading to inaccurate iden-
89 tification of apparent transport parameters [*Sanchez-Vila et al.*, 1996]. Counterexamples
90 are provided from 2D simulations with very large $\ln K$ variance (e.g., [*Le Borgne et al.*,

2008] or when inclusion models are used (e.g., [Fiori et al., 2006]). Tailing however has also
been observed in experiments with low $\ln K$ variance and distributions of K different from
embedded inclusions, such as in the 3D laboratory experiments (e.g., [Fernàndez-Garcia
et al., 2002]) or field-scale tracer tests (e.g., [Riva et al., 2008]). A comparison between
unconditional 2D and 3D Multigaussian numerical simulations by Pedretti et al. [2013]
indicates that 2D ADE-based simulations fail to reproduce tailing, while 3D ADE-based
simulations do produce such tailing, under convergent radial flow.

The inability of unconditional 2D fields to generate anomalous transport may be related
with the poor ability of 2D configurations to reproduce important connectivity patterns
that exist in typical aquifers. For example, some authors obtained anomalous distributions
of BTCs from 2D simulations after manipulating unconditional simulations to increase
transport connectivity (e.g., [Zinn and Harvey, 2003; Willmann et al., 2008]), thus effec-
tively removing the idea of statistical stationarity from the system. These authors showed
that connectivity not only affects the advection porosity, but also influences the choice of
mass-transfer parameters in a theoretical formulation of transport based on overlapping
mobile and immobile pore fractions (defined below). Interpretations of experiments by
Fernàndez-Garcia et al. [2002] using a single porosity model show that anisotropy and
connectivity are jointly two of the most important features controlling advection porosity
in CFTTs. The issue of connectivity has been largely debated in recent years, although,
to date, no unique quantifiable definition of connectivity exists (e.g., [Renard and Allard,
2013]).

Another complication relates to the injection-extraction distance (R) of CFTTs and
the nonstationary flow that is typical in most experiments. As reported by Gelhar [1993],

114 tracer tests are usually performed under highly non-ergodic conditions, both because flow
115 is radial in two-well settings and because R is often on the order of a few horizontal
116 integral scales associated with the soil heterogeneity (I_x). However, for practical theo-
117 retical reasons (e.g. [*Dagan*, 1989; *Rubin*, 2003]) the tendency has been to build models
118 of solute transport assuming ergodicity, which may not be a reasonable assumption as
119 ergodicity can require an R on the order of tens to hundreds times I_x , even for uniform
120 flow [*Matheron*, 1967].

121 In the recent paper by *Pedretti et al.* [2013], a set of 3D unconditional Multigaussian
122 numerical simulations of radial convergent transport in heterogeneous media showed that
123 anomalous transport, displayed by highly asymmetric depth-integrated BTCs, could be
124 associated with transport stratification. This was particularly evident when R was on
125 the order of I_x . The ratio between these two variables can be seen to largely impact
126 not only the degree of asymmetry of the BTCs (i.e. the departure from ADE-predicted
127 symmetric distributions, measured as the dimensionless time difference between the BTC
128 concentration peak and its center of mass), but also the apparent power-law decrease of the
129 BTC after the concentration peak. *Pedretti et al.* [2013] also indicate that the transverse
130 dispersivity at the local scale (i.e., the Peclet number at the scale of a numerical grid
131 cell) may have a small impact on the slope of apparent power-law tailing on the late-time
132 BTCs and a stronger impact on the BTC's degree of asymmetry. However, in the latter
133 case, an insufficient number of simulations were conducted to confidently evaluate the
134 dependence of slope and degree of asymmetry with local dispersivity. A similar analysis
135 on the influence of the flow velocity on the mass-transfer parameters was reported by
136 *Sharifi Haddad et al.* [2012].

137 Both late-time power-law slopes and the degree of asymmetry are important indicators
138 used for the inference of microscale heterogeneity using so-called *non-Fickian* or *non-local*
139 models, a class of effective models which have emerged with the intent of better describing
140 transport at intermediate to large scales. These methods include models based on multi-
141 porosity domains, which we focus on in this paper due to their wide use. Conceptually
142 multi-porosity models are based on the existence of heterogeneities at the microscopic
143 level that exchange mass between fast (or mobile) aquifer zones and slower (or immobile)
144 aquifer zones by mass transfer. One of these models, the multi-rate mass transfer (MRMT)
145 model conceptualizes the aquifer as a multi-porosity system made up of a continuum
146 superposition of a mobile and multiple immobile domains [*Haggerty and Gorelick, 1995;*
147 *Zinn and Harvey, 2003*]. Each immobile domain exchanges mass with the mobile domain
148 at a different rate. The ratio of the sum of all immobile porosities and the mobile porosity
149 defines a parameter called the *capacity coefficient* (β). This parameter controls the relative
150 amount of mass that is present in the late-time BTC tail [*Pedretti et al., 2013*]. The
151 superposition of rates at which mass exchanges between these zones is described by a
152 functional parameter called the *memory function* [*Carrera et al., 1998*]. MRMT is also
153 popular because chemical reactions can be readily incorporated [*Donado et al., 2009;*
154 *Willmann et al., 2010*].

155 Mass-transfer models are widely used because of their versatility and ability to fit BTC
156 tailing. However, mass transfer is a short name for a suite of complex physical processes
157 linked to the existence of randomly distributed microscopic zones characterized by dif-
158 ferent pore-water velocities. Macroscopic evidence of mass-transfer processes includes
159 heavily-tailed BTCs observed during tracer tests; this phenomenological evidence has led

160 some authors to postulate that heavily-tailed BTCs may indicate the presence of mass-
161 transfer processes at local scales. Nonetheless other processes can lead to tailing (e.g.
162 advection in heterogeneous media) and can be confused with mass transfer. Additionally,
163 a concrete relationship between the mathematical and aquifer physical parameters can
164 be built only for a relatively limited number of cases, for instance when mass transfer
165 is dominated by diffusion-like processes [*Nkedi-Kizza et al.*, 1984; *Haggerty and Gorelick*,
166 1995; *Carrera et al.*, 1998]. In this case, experimental evidence has validated this approach
167 (e.g., [*Gouze et al.*, 2008; *Zhang et al.*, 2007]), and its use as a predictive tool is physically
168 justifiable.

169 When tailing occurs in advection-dominated field experiments, a common situation
170 widely observed in field and numerical experiments (e.g., [*Becker and Shapiro*, 2000; *Zinn*
171 *and Harvey*, 2003; *Fernàndez-Garcia et al.*, 2004; *Pedretti et al.*, 2013]), mass-transfer-
172 based formulations can be still used for fitting purposes but mass-transfer parameters
173 become empirical, or *apparent* as they are not directly linked to any measurable physical
174 property of the subsurface. This is generally why their validity as predictive tools is limited
175 and why their use as effective upscaling approaches is highly criticized (e.g., [*Neuman*
176 *and Tartakovsky*, 2009]). Despite this, the possibility of generalizing non-Fickian model
177 descriptions as practical predictive tools is highly appealing due to their relative simplicity.
178 Several authors (e.g., *Zinn and Harvey* [2003]; *Willmann et al.* [2008]; *Flach* [2012]) have
179 numerically explored phenomenological links between simulated aquifer properties and
180 apparent parameters of non-Fickian upscaled models, but their general conclusion is that
181 no unique solutions to fit model data exists. Experimental attempts to deal with this

182 issue have also been documented (e.g., [Zinn *et al.*, 2004]), and while powerful due to
183 methodological and technical limitations the results were somewhat unsatisfactory.

184 To date it is generally not possible to establish a direct link between aquifer parameters
185 and apparent mass-transfer parameters for advection-dominated problems. The aim of
186 this paper is to show that it is possible to find a phenomenological correlation between
187 the statistical anisotropic K distribution characterizing heterogeneous porous media at
188 intermediate scales and the anisotropic distribution of certain nonlocal parameters under
189 a convergent flow scheme. We limit our paper to the analysis of the capacity coefficient
190 β , which is a parameter based on the concept of mobile and immobile porosity; recall
191 that porosities have been found to display directional properties in anisotropic aquifers
192 [Sanchez-Vila and Carrera, 1997] under radial convergent flow.

193 Specifically, this paper aims to address the following two questions:

- 194 • Does the apparent β depend upon anisotropy when estimated from CFTTs, as ad-
195 vection porosity does in single-porosity models?
- 196 • What physical features control β ?

197 Our approach is based on numerical models that solve for flow and transport in het-
198 erogeneous formations characterized by known anisotropic statistics, with a numerical
199 setup similar to the one used by Pedretti *et al.* [2013]. The paper is structured as fol-
200 lows. In Section 2, we develop our model and define the moment-based approach to find
201 approximate estimates of β from the numerical BTCs. In section 3 we define important
202 dimensionless variables. In sections 4 we discuss statistical features controlling the value
203 of β with discussion linking connectivity and β in section 5. Section 6 focuses on results
204 from a single realization and conclusions are presented in section 7.

2. Directional and anomalous behavior of BTCs in anisotropic aquifers

2.1. Conceptual model and numerical setup

205 Let us consider that CFTTs are performed in heterogeneous formations characterized
206 by a oriented statistical distribution of the hydraulic conductivity, with similar patterns
207 to the geological structures shown in Figure 1 (cases A and B). We assume that the tests
208 are performed with ideal conservative tracers. A passive well (e.g., a piezometer) is used
209 to inject the compounds and an active well, located at a planar distance (R), is used to
210 capture the tracer over time. We assume both wells to be fully screened along the entire
211 vertical section of the aquifer, which has constant thickness (b). The active well pumps
212 at a constant imposed rate (Q), until steady state flow conditions are attained before the
213 tracer is injected. If R is small and Q is large, a typical natural background flow can
214 be neglected and a purely convergent flow is assumed. The tracer test is performed by
215 introducing a finite and known mass of solute (M) as a pulse input from the passive well,
216 at a rate that does not affect the local groundwater level around it; we use a flux-averaged
217 injection scheme [*Parker and Van Genuchten, 1984*]. The depth-integrated flux-averaged
218 concentration is measured at the active well to obtain a breakthrough curve (BTC).

219 This conceptual setup can be modeled numerically following the methodology presented
220 by *Pedretti et al.* [2013]. Full details regarding the numerical implementation of the log-
221 transformed K fields, the numerical flow solution, and the evaluation of the BTC from
222 a particle tracking algorithm are available therein. All fields are made up of a three-
223 dimensional regular mesh of 251x251x100 cubic cells of unit volume. The log-transformed
224 hydraulic conductivity ($Y = \ln(K)$) values in each individual realization are drawn from
225 a multigaussian distribution with zero mean, finite variance $\sigma_Y^2 = 4$ and anisotropic ex-

226 exponential variograms. Within each cell Y is isotropic ($Y_x = Y_y = Y_z$), with the exception
 227 of the active well location at the center of the domain, where a vertical local K value five
 228 orders of magnitude larger than the mean value is imposed. A sink term is imposed at
 229 the bottom of the well, where the discharge rate is fixed. The use of high vertical local K
 230 in the cells corresponding to well position in the other layers simulates a fully-penetrating
 231 well, without the need of imposing additional boundary conditions. Additional details
 232 can be found in *Pedretti et al.* [2013].

233 All simulations are carried out with a total constant porosity $\phi = 0.1$ and local disper-
 234 sivity $a = 0.25$ (isotropic). These parameters control characteristic dimensionless numbers
 235 such as the Peclet numbers), which can influence on BTC shapes (e.g., [*Riva et al.*, 2008])
 236 and/or on β (e.g. [*Pedretti et al.*, 2013]). We do not present their specific influence in this
 237 context, as its qualitative influence can be understood from the results of cited papers.
 238 We leave detailed quantification open for future investigations.

239 To reproduce domains similar to those in fig. 1, we run stochastic simulations with
 240 different integral scales in the x, y, z directions (respectively I_x, I_y and I_z). Defining the
 241 anisotropy ratio between pairs of integer scales as $\epsilon_{ij} = I_i/I_j$, we focus on two sets of
 242 geometries:

- 243 1. Fields (A) with enhanced correlation along a horizontal direction y ($I_y=40$, $I_x=4$,
 244 and $I_z=4$, corresponding to $\epsilon_{xy} = 0.1$, $\epsilon_{xz}=1$, $\epsilon_{yz}=10$);
- 245 2. Fields (B) with large correlation along two directions, those marked by the plane yz
 246 ($I_y=40$, $I_x=4$, and $I_z=40$, corresponding to $\epsilon_{xy} = 0.1$, $\epsilon_{xz}=0.1$ and $\epsilon_{yz} = 1$).

247 Examples of these fields are illustrated in Figure 2, where it can be seen on the top-left
 248 that field (A) corresponds to a geologic setting similar to the one reported on the top-left
 249 of Fig. 1, while field (B) more closely resembles the outcrop in the top-right of Fig. 1.

250 Transport is simulated using a random-walk approach (using code RW3D [*Fernández-*
 251 *García et al., 2005; Salamon et al., 2007*]). At time zero particles are introduced into the
 252 system as a vertical line using a flux-weighted scheme. Figure 2 highlights the 8 specific
 253 injection locations that are chosen for analysis of the BTCs:

- 254 • Injection points $U1, U2, U3, U4$ are oriented collinear with the y-axis, at the same
 255 x-coordinate of the well and at distances respectively of $R = 5, 12.5, 25, 75$ units from the
 256 well;

- 257 • Injection points $R1, R2, R3, R4$ are oriented collinear with the x-axis, at the same
 258 y-coordinate of the well and at distances respectively of $R = 5, 12.5, 25, 75$ units from the
 259 well.

Using particle tracking methods, depth-integrated time-dependent concentrations
 ($C(t)$) are measured at the extraction well (i.e. the BTCs); these are equivalent to particle
 density functions (\hat{p}) estimated from the arrival time distributions of particles at the well.
 This is achieved assuming that

$$\hat{p}(t) = \frac{QC(t)}{\int QC(t)dt}. \quad (1)$$

260 To resolve the curves adequately without using a prohibitively large number of par-
 261 ticles we used a kernel density estimator (*KDE*) approach described in *Pedretti and*
 262 *Fernández-García* [2013]. This technique is based on optimized Gaussian kernel functions
 263 that reconstruct BTCs from a limited particle dataset. *KDE* is especially effective in
 264 capturing features of heavy-tailed BTCs in an efficient manner. After some preliminary

runs it was found that adequate, converged results were obtained with $N_P = 10^4$ particles
 and an adaptive weighting factor $\alpha = 0.5$ (see *Pedretti and Fernàndez-Garcia* [2013] for
 details on the selection of α).

2.2. Definition and estimation of the directional capacity coefficient

A common approach to upscale anomalous transport in heterogeneous aquifers is by
 means of MRMT solutions. The models assume the presence of different volumes within
 an individual cell where water either flows (mobile zones) or does not flow (immobile
 zones). There is a linear mass transfer of solutes between these zones and each zone
 is characterized by a particular mass-transfer coefficient. The flexibility of this model
 arises from the distribution of the mass-transfer coefficients, which weight the relationship
 between immobile and mobile zones over time (i.e. the temporal storage of solute in the
 immobile zones). Several distributions have been postulated to include multiple domains
 with continuous or discrete distributions of mass-transfer parameters (e.g., *Haggerty and
 Gorelick* [1995]; *Cameron and Klute* [1997]; *Carrera et al.* [1998]; *Haggerty et al.* [2000]).
 A mathematical formulation for a multirate mass-transfer model under radial coordinates
 (r-MRMT) reads

$$\frac{\partial C_m}{\partial t} + \beta \Gamma(x, t) = v_m(r) \frac{\partial C_m}{\partial r} + \frac{a_r v_m(r)}{r} \frac{\partial}{\partial r} \left(\frac{1}{r} \frac{\partial C_m}{\partial r} \right) \quad (2)$$

where β is the capacity coefficient, which is given by $\beta = \phi_{im}/\phi_m$. C_m is the solute
 concentration in the mobile (flowing) zone, a_r is the (longitudinal) dispersivity, v_m is a
 representative (mean) mobile velocity and $\Gamma(x, t)$ is a sink-source term which accounts
 for the mass-transfer from and to the immobile zones. From (2), β sets the amount of
 mass that can be stored in the immobile domain. It does not control the shape of the

285 concentration curve at late-times; this is controlled by the memory function embedded in
286 Γ (e.g. *Carrera et al.* [1998]). In general the time corresponding to the peak in a BTC
287 is controlled by the value of ϕ_m , while the mean arrival time is controlled by the total
288 porosity ($\phi_m + \phi_{im}$). Note that alternative and equally valid formulations may embed β
289 into the memory function; however, we prefer here to separate them for the sake of our
290 analysis, as we mainly focus on the behavior of β .

291 Specifically, our focus here is on finding directional patterns of the apparent β from
292 numerical simulations performed in fields (A) and fields (B) (Fig. 2). One possible way of
293 obtaining β would be to fit each of the experimental random BTCs by solving (2) directly
294 to obtain a distribution of apparent best-fitting parameters. This approach is challeng-
295 ing and can result in inaccurate solutions as solving (2) is not always straightforward.
296 Analytical solutions (e.g., *Haggerty and Reeves* [2002]) are usually restricted to a finite
297 combination of parameters and can rely on numerical inversion of Laplace transformed
298 solutions, which are prone to numerical instabilities. Other numerical techniques can be
299 adopted instead (e.g., *Silva et al.* [2009]) but this can be computationally burdensome.
300 Moreover for CFTTs, BTCs (e.g., *Pedretti et al.* [2013]) can display very different shapes
301 from the typical BTCs that are implemented in existing codes (e.g., *Haggerty et al.* [2000]).

302 As an alternative to the full numerical solution we propose an approximate, faster
303 approach based on travel time moments that yields a unique value for β for each BTC.
304 Because the first moment of solute travel time depends exclusively on β and not on
305 the mass-transfer rate coefficients (*Valocchi* [1985]; *Goltz and Roberts* [1987]; *Harvey and*
306 *Gorelick* [1995]; *Rubin et al.* [1997]), β can be directly found from BTCs using the ratio
307 between the first moment and the mean mobile time (t_{MT}) as

$$\beta = \frac{\mu_t^1}{t_{MT}} - 1, \quad (3)$$

308 where μ_t^1 is the first-moment of the travel time distribution defined as (*Aris* [1956])

$$\mu_t^1 = \frac{\int tC(t)dt}{\int C(t)dt}. \quad (4)$$

309 The derivation of (3) is presented in Appendix A. Note that this solution is not practical
 310 for our purposes since it requires the estimation of t_{MT} from the BTCs. The latter is
 311 an additional apparent parameter that would be obtained after model fitting using (2)
 312 (similar to a fitting procedure to obtain β , as explained above). It is convenient here to
 313 assume that $t_{MT} \approx t_m$ (i.e. the mean mobile time being similar to the peak time). This
 314 approximation results in

$$\beta \approx \frac{\mu_t^1}{t_m} - 1. \quad (5)$$

315 This approximate solution is more versatile as it involves t_m , which is more easily and
 316 uniquely identifiable from the estimated BTCs, and avoids a fitting procedure using (2).
 317 We tested and successfully verified the accuracy of this approximation against a classical
 318 fitting procedure. A small subset of illustrative examples are reported in Appendix B -
 319 Supplementary Attached Material.

3. Dimensionless variables

320 To compare results let us define the following dimensionless variables. A dimensionless
 321 time, t_c , is calculated as

$$t_c = t/t_{adv}, \quad (6)$$

322 where

$$t_{adv} = \frac{\pi b \phi R^2}{Q} \quad (7)$$

323 represents the mean advection time for a solute to travel within an homogeneous cylin-
 324 drical aquifer under convergent flow conditions using Dupuit's assumption (e.g., [Moench,
 325 1989]). Recall that throughout the simulations, porosity is assigned a deterministic
 326 spatially-constant value ($\phi = 0.1$).

327 Let us also introduce the normalized horizontal injection-extraction distance, defined as

$$r_\lambda = \frac{R}{I_r} \quad (8)$$

328 where I_r is the integral scale collinear with the injection-extraction axis. For injection
 329 locations $R1$ to $R4$, this means $I_r = I_x$, while for injection locations $U1$ to $U4$, this means
 330 $I_r = I_y$. It is also important to compare the relative length of the injection line (which
 331 corresponds to the model thickness, b) with the vertical integral scale, I_z . A variable, L_z ,
 332 is defined as

$$L_z = \frac{b}{I_z} \quad (9)$$

333 The larger L_z , the more the solute is injected through a few preferential flow path, such
 334 as in fields (A); conversely, the smaller L_z , the more homogenized is the injection, such
 335 as in fields (B).

4. Statistical features controlling the spatial distribution of β

336 Our first goal was to understand if the apparent β depends on anisotropy when estimated
337 from CFTTs. To achieve this, it is useful to first indicate whether useful phenomenological
338 evidence can be obtained from statistical inference. 250 realizations of each field (A) and
339 (B) were produced. In each one particles were injected at different points drawn from a
340 grid of points representing fully penetrating piezometers and tracked until they reached
341 the well. The value of β was then estimated for each BTC using (5). From this a 2D
342 map was drawn indicating β at each injection point. To emphasize the widely contrasting
343 values found and visually highlight the anisotropic structures, we present results as the
344 logarithm (base 10) of the capacity coefficient (denoted $\log(\beta)$).

345 The two resulting maps for the ensemble average of the log-transformed capacity coeffi-
346 cient, $E(\log(\beta))$, from the 250 simulations of field (A) and field (B) are plotted in Figure
347 3. The structure of both maps is clearly and qualitatively anisotropic. Only at injection
348 locations close to the pumping well is no apparent anisotropic structure is visible. This
349 is likely a combination of local isotropy of the blocks and the resolution of the numerical
350 grid (discussed in more detail further on). From a quantitative perspective, although both
351 $\log(\beta)$ maps are anisotropic, they show very distinct values, as emphasized by the use of
352 a common color scale; note for instance that the $\log(\beta)$ map for field-type (A) displays
353 fewer negative $\log(\beta)$ values, while such negative values are more common in field-type
354 (B).

355 The quantitative difference between the maps presented in Fig. 3 is associated with
356 the different vertical integral scales L_z values, which are 10 times smaller in fields (A)

357 as compared to those of fields (B). From a statistical perspective, this means that the
 358 ensemble statistics of fields (A) should display less variability than the ones of fields (B).

359 The distribution of the second moment of the experimental Monte Carlo distribution
 360 (not shown here) indicates that, while $E(\log(\beta))$ is highly structured for both fields, this
 361 is not the case for the variance ($\sigma_{\log(\beta)}^2$). We observed no significant spatial organization
 362 for $\sigma_{\log(\beta)}^2$ values in either fields (A) and fields (B); the difference is found in the average
 363 values ($\overline{\sigma_{\log(\beta)}^2}$) which was found to be smaller for fields (A) ($\overline{\sigma_{\log(\beta)}^2} = 0.80$) with respect
 364 to those for fields (B) ($\overline{\sigma_{\log(\beta)}^2} = 1.12$). Again, while the number of realizations (250) used
 365 to obtain these numbers might be considered small, we want to stress that the objective
 366 was to find whether the maps of β displayed a spatial structure at all, rather than finding
 367 the actual values of β at given locations.

368 From these results it should be clear that from a statistical perspective, there is a clear
 369 dependence of the spatial anisotropic organization of $\log(\beta)$ on the structure of $\ln K$.
 370 However, this result alone does not really explain what physical processes controls β for
 371 a given tracer test performed at a given location (x, y) . A deeper understanding of this
 372 would be fundamental to understanding what soil parameters actually control the size of
 373 the mass-transfer capacity coefficient, which would give additional insights to understand
 374 how one might begin to build predictive versions of a MRMT model. This is explored in
 375 the following sections.

5. Exploring the role of connectivity in controlling β

376 From the previous section we know that apparent β values derived from individual tracer
 377 tests depend on L_z , but also on r_λ , because the structure of $\log(\beta)$ depends on whether the
 378 injection-extraction direction is collinear or orthogonal to the main planar anisotropic axis.

379 When r_λ is small and/or L_z is large, transport can be highly nonergodic, as the solutes
380 sample only a relatively small portion of the heterogeneity between the injection and the
381 extraction well. From a qualitative perspective, this gives rise to connected structures,
382 which may influence the distribution of particle travel times.

383 Some of these concepts have been recently discussed by *Pedretti et al.* [2013], who ana-
384 lyzed the apparent joint effects of stratification and connectivity due to lack of ergodicity
385 in these systems. In *Pedretti et al.* [2013], in addition, it was shown that the concentration
386 peaks obtained after analyzing particle travel times transported over different layers in 3D
387 formations are very representative of the total connectivity of the system from the injec-
388 tion point to the extraction well, as related by the system stratification. Similar concepts
389 are used here to explain the quantitative link that exists between directional connectivity
390 and the apparent directional capacity coefficient.

391 This part of the study is based on the concept of '*point-to-point connectivity*'
392 (e.g., [*Knudby and Carrera, 2006; Trinchero et al., 2008*]). For the specific case of con-
393 vergent radial transport, this method postulates that a *dynamic* connectivity indicator
394 [*Renard and Allard, 2013*] can be obtained from the relative temporal scaling of the
395 BTCs peak time (t_m) in a heterogeneous medium compared to an equivalent homoge-
396 neous medium. Recall the definition of dimensionless time used in this analysis (6); in an
397 homogeneous field all BTCs plotted on a double-log plot would be symmetric around the
398 concentration peak, which would occur at $t_c = 1$. Similarly, connectivity can be quantita-
399 tively measured as the relative position of t_m with respect to $t_c = 1$: the shorter the peak
400 time ($t_m/t_c < 1$), the more hydraulically connected are the injection-extraction wells; and
401 vice versa, the larger the peak time ($t_m/t_c > 1$), the less connected are these two locations.

402 We direct the interest reader to the cited works for a more exhaustive description of these
 403 concepts.

5.1. Qualitative analysis

404 First let us focus on qualitative aspects of the BTCs (from which β is obtained) asso-
 405 ciated with two orthogonal injection points $R4$ and $U4$. These are located at the same
 406 distance from the well ($R=75$ cells), but have different r_λ values. For these cases 1000 re-
 407 alizations are simulated, and all the BTCs for these two injection locations are depicted in
 408 Figure 4. Plots are presented one a double-log axis to emphasize any anomalous late-time
 409 behavior.

410 On the top-left of Fig. 4 we plot the BTCs associated with injection point $R4$ ($r_\lambda =$
 411 $r/I_x = 18.75$) in fields of type (A) ($L_z = 25$). As one might expect, we observe that
 412 most curves are located around $t_c = 1$ (marked by the vertical dashed line), and only a
 413 few show significantly different peak times. This also means, consistent with the above
 414 definition of connectivity, that from this graph only a few simulations offer a noticeable
 415 deviation from the homogeneous case, and thus there is a limited effect of connected
 416 features. For illustrative purposes, we highlight with different colors three individual
 417 BTCs, representing respectively highly connected, mildly connected and less connected
 418 simulations. The red line highlights the BTCs from a realization showing one of the
 419 shortest peak times ($t_c \ll 0.1$) found in the ensemble of BTCs, indicating the highest
 420 degree of connectivity among all cases. In this well-connected case, the BTC displays a
 421 fast early arrival time followed by a prolonged late-time tailing behavior. Tailing in this
 422 case is defined as the persistent slope observed on these plots. Tailings seems to scale as
 423 straight line in double-log plots, thus similar to power-law distributions; however, since

424 most of the BTCs span only a few logarithmic time cycles, caution should be taken when
 425 inferring a power-law distribution in this narrow time interval (e.g., *Clauset et al.* [2007]).

426 A similar behavior can be seen on the BTC represented by the blue line. Here, the peak
 427 time is closer to $t_c = 1$ than for the red curve, and the anomalous tailing is less defined
 428 than in the previous case (indeed for this case, no apparent power-law behavior can be
 429 easily identified). In the other highlighted realization, the peak of the black BTC occurs
 430 at $t_c > 1$ and the shape of the curves appear more symmetric (like an homogeneous case).
 431 The behavior of the latter curve is also representative of the majority of BTCs within the
 432 ensemble, thus indicating that only a few cases display anomalous behavior, defined by
 433 the nonsymmetric nature of the BTCs.

434 A different behavior is observed when the injection location switches to U4 ($r_\lambda = r/I_y =$
 435 1.88) on the same fields (A). These plots are shown at the top-right of Figure 4. The solute
 436 travels less than 2 integral scales to the extraction well. The main difference with respect
 437 to the curves when the tracer is injected at R4 is that most of the BTCs display peak
 438 times shorter than $t_c = 1$ (indicating higher connectivity), and most of them also display
 439 heavy tailing. Looking at the same four fields discussed for the previous location, it can
 440 be seen the peak times of all these BTCs are lower than $t_c = 1$. Even for this location
 441 it can be seen than the qualitative relationship between peak time (connectivity) and
 442 development of asymmetric tailing can be observed, meaning that, also for this case, as a
 443 general rule simulations where the peak time is smaller are also those displaying stronger
 444 tails.

445 On the bottom of Figure 4 we show the BTCs obtained from injection locations R4 and
 446 U4, respectively, for field (B) ($L_z = 2.5$). Here the effect of the vertical homogenization

447 of the injection can be seen, observing that at R4 BTCs look more symmetric in field (B)
448 than their counterparts in field (A). However, BTCs from point U4 still display the strong
449 effects of connectivity. We highlight three specific and representative cases for fields (B).
450 Violet and light-blue curves represent fields where BTCs are quasi-symmetric for both
451 R4 and U4 injection locations. It can be seen that at U4 the violet BTCs display, at
452 very late-time, anomalous tailing for a very limited time extent. On the other hand, the
453 green line at U4 displays strong anomalous behavior with a heavy-tailed distribution; once
454 again, this is the case with the highest degree of connectivity from this ensemble.

5.2. Quantitative analysis

455 We qualitatively observed from the previous section that larger nonsymmetric distribu-
456 tions (larger *beta*) are found when connectivity was also larger (lower t_m). To seek a more
457 quantitative description of the relationship between β and connectivity, let us first observe
458 the statistics of the distribution of the three main transport variables considered in this
459 analysis (β , t_m and μ_t^1) for locations R1 to R4 and for locations U1 to U4, for both fields
460 (A) and (B). The application of a chi-squared test suggests that all these distributions
461 are log-normal (α -level of significance equal to 5%), so that for each parameter we report
462 the statistics of the log-transformed counterpart.

463 The complete results of these statistics are reported in Tables 1 and 2 - Supplementary
464 Attached Material. We observe that these data have large uncertainty around the mean
465 values (reflected by the large *CV* value). This is true particularly for fields (B) (e.g. at
466 point U3), confirming that the large integral scales applied both in the horizontal and the
467 vertical directions relative to injection distance from the well and domain thickness result
468 in lack of ergodicity in the transport solutions, making the ensemble a somewhat mean-

469 ingless measure with poor applicability for predictive purposes. On the other hand, for
470 fields (A), such variability is much lower, and the ensemble means are more representative
471 of the BTCs recorded in each realization than in the previous case.

472 Comparing how these variables are correlated by pairs, we can observe that a robust
473 relationship appears to exist between β and the connectivity indicator t_m for fields (A) and
474 position *R4* (fig. 5-1). The best-fit model using a linear least-square regression method
475 for this correlation turned out to be an exponential model with a Pearson's coefficient of
476 $R^2 = 0.61$ and a low root mean square error (RMSE). The correlation highlights that the
477 higher the connectivity, the larger β ; and vice-versa. That means that a weak (apparent)
478 separation of transport in mobile and immobile zones occur for less connected points; as
479 connectivity increases (shorter t_m), β increases, indicating a higher degree of (apparent)
480 separation in mobile/immobile subdomains.

481 This inverse dependence between β and connectivity is still visible for injections associ-
482 ated with point *U4* in fields (A) (fig. 5-2), but with a much higher degree of uncertainty
483 (larger RMSE and much smaller R^2 than the *R4* case). In this case, all values are found
484 between $\beta = 1$ and $\beta = 10$. Another important aspect shown in Figures 5-3 and 5-4 is
485 that β appears very poorly correlated with μ_t^1 , even though figures 5-5 and 5-6 indicate
486 that there exists a strong correlation between the t_m and μ_t^1 . The fact that t_m and β are
487 better correlated than μ_t^1 and β is linked to the propagation of errors of the correlation
488 between t_m and μ_t^1 . This issue is consistent with our analysis, since t_m is a better estima-
489 tor of connectivity than μ_t^1 , and connectivity has greater influence on β than the position
490 of the center of mass. This is similar to the observations drawn the individual realization
491 analysis, which will be provided in the next section.

492 For fields (B) (Fig. 6), the correlation between variables for both injection locations for
493 $R4$ and $U4$ is generally worse. In this field, no significant correlation is found between
494 β and connectivity (Figs. 6-1 and 6-2), nor between β and μ_t^1 (Figs. 6-3 and 6-4).
495 Similar to what was observed for field (A), on the other hand, there is a solid relationship
496 between t_m and μ_t^1 (Figs. 6-5 and 6-6). This is explained again by the fact that the
497 realizations from fields (B) display much less vertical variability of K . Particle injection
498 and transport is much more homogenized, on average, for fields (B) than in fields (A).
499 This also indicates that the flux-weighted injection that happens preferentially in small
500 channels (low L_z) rather than in more homogenized formations (high L_z) is a fundamental
501 aspect controlling the dependence of β on the connectivity.

502 This general behavior is in line with other previous studies on anisotropic formations un-
503 der uniform flow, which pinpoint the relationship between tailing and statistical anisotropy
504 of the system (e.g. [Guswa and Freyberg, 2002]). Our results extend the analysis by Pe-
505 dretti *et al.* [2013] and Pedretti and Fiori [2013] which highlighted the importance of
506 stratification on tailing under convergent radial flow. In Pedretti *et al.* [2013] it was ob-
507 served that the formation of tailing on BTCs is controlled primarily by the dimensionless
508 injection distance r_λ . When $r_\lambda \approx 1$, such as in the case of injections $U4$, particles travel
509 only a few integral scales and are thus subjected to plume stratification. As the difference
510 in connectivity among layers becomes more important, the solute tends to be more strati-
511 fied, giving rise to a larger separation of the peak time from the center of mass of the plume
512 (i.e. β). As the injection distance approaches 0, the injected plume becomes perfectly
513 stratified and β is largest. The anisotropic distribution of β is therefore a consequence of
514 the ability of the injected solute to be stratified around the well.

515 Consequently, we observed here that the physical link between β and K is related
516 to the statistical heterogeneity scales, which control the tradeoff between vertical mix-
517 ing and transport stratification. Vertical mixing tends to homogenize the transport and
518 thus renders BTCs more symmetric; this occurs when the dimensionless injection dis-
519 tance $r_\lambda \gg 1$. On the other hand, the variable connectivity of the layer composing
520 the formation (intimately related to stratification) tends to maintain a separation of the
521 contribution to each single layer of the depth-integrated BTCs, as explained in *Pedretti*
522 *et al.* [2013]; this occurs when $r_\lambda \sim 1$. In addition, the shorter the injection distance
523 compared to the vertical domain size (fields (A)), the more significant this stratification
524 effect is; therefore, the vertical dimensionless injection length also plays a fundamental
525 role in determining the ability of the system to separate apparent mobile and immobile
526 transport under convergent radial flow.

6. What happens in an individual random realization?

527 From our observations so far we conclude that there exists a correlation between connec-
528 tivity and β in a statistical sense. From a qualitative perspective, our conclusion matches
529 those of *Zinn and Harvey* [2003] and *Willmann et al.* [2008], among others, but here we
530 have also quantified this dependence. This is a critical issue because it provides a physical
531 explanation for a mass-transfer parameter, β , derived in advection-dominated problems.
532 This is promising in the path towards improving the predictive capacity of models in these
533 types of transport regimes.

534 To test how generally true our findings are and to what extent they hold, we now analyze
535 what happens in an individual realization. We chose one random realization selected from
536 the ensemble of field (A). We ran a CFTT with an injection at each (x,y) grid location

537 and explored the correlation of β , t_m and μ_t^1 . For the single realization case we compared
538 the values obtained for all (x,y) pairs, including those points close to the well.

539 The resulting β map for this field is shown in Fig. 7-2. For comparison purposes we
540 also plotted the vertically-averaged $\ln K$ for this chosen field (Fig. 7-1), as well as the
541 maps for μ_t^1 (Fig. 7-4) and t_m (Fig. 7-3). The latter represents also the "point-to-point
542 connectivity" map, as point-to-point connectivity is directly related to the inverse of the
543 BTC peak time, as explained in the previous sections. Visually, all three plots display
544 certain structural similarities, although μ_t^1 appears much smoother than the other two;
545 this is due to the fact that the average time taken by plume to migrate from the injection
546 to the extraction point is not only influenced by the irregular random shape of preferential
547 channels (fast flow zones) but is dispersed into all the less mobile zones between the two
548 points in a more continuous way.

549 Larger β and t_m values in the maps show a channeled structure along the y -axis (brighter
550 and darker colors respectively in the relative maps, also highlighted by the green ellipse
551 drawn on the maps), which is also the main preferential statistical correlation of Y used
552 to build this field. Conversely, lower β values are found in the presence of larger BTCs
553 peak times, such as in the lower-left regions of these maps.

554 To quantify our purely visual inferences of correlations in the previous paragraph, in
555 Figure 8 we plot bivariate plots of β , t_m and μ_t^1 and present best-fit models of this data (as
556 for the ensemble analysis). It was found that a power-law function is the best-fit model
557 when t_m is plotted against the two other variables. However, the Pearson coefficient R^2 is
558 low, indicating large dispersion of data around the power-law trend. Also, no significant
559 correlation between β and μ_t^1 was found, indicating that the distribution of advection time

560 does not control the distribution of the capacity coefficient as significantly as connectivity
561 does. This is despite the fact that advection and mobile times have a much stronger
562 correlation, as shown in the bottom plot of Figure 8.

563 As such, connectivity is the primary responsible factor for the distribution β , also in this
564 individual realization. This suggests that it is the physical parameter that most strongly
565 controls the apparent mass-transfer parameter.

566 Single-realization correlations are smaller than those of the ensemble. Measurements
567 corresponding to all locations in the map are plotted together, while in the ensemble
568 analysis we focused on several random outcomes from a few injection locations; the de-
569 velopment of tailing due to heterogeneity is largely controlled by the relative injection
570 distance for CFTTs, as shown by *Pedretti et al.* [2013].

7. Conclusions

571 Upscaling of anomalous transport in heterogeneous formations under radially conver-
572 gent flow is a complex issue; it is important for making practical and effective decisions
573 for risk assessment and remediation of polluted heterogeneous aquifers [*Bolster et al.*,
574 2009; *de Barros et al.*, 2011]. We conducted a numerical study to check the existence
575 of phenomenological links between the capacity coefficient β (which is an important pa-
576 rameter used in common upscaling approaches), and the directional-dependent statistical
577 correlation of the natural log-transformed hydraulic conductivity, Y . This link is only
578 apparent (hence the name of "apparent capacity coefficient") since formally speaking β
579 is mathematically based on diffusive-like mass transfer processes giving rise to anomalous
580 transport, while the latter occurs in our analysis under advection-dominated conditions.

581 We developed a quick and efficient method to estimate β , demonstrated in appendix B,
582 which is expressed as the ratio between the first moment of the arrival time distribution
583 and the concentration peak time from each breakthrough curve. The latter provides
584 an indication of "point-to-point connectivity", i.e., how fast/slow the response time is
585 between the injection and the extraction locations during a convergent-flow tracer tests.
586 We measured this parameter after reconstructing BTC peak times from particle travel
587 time distributions after being injected at different locations in a convergent flow radial
588 setup.

589 Our analysis spanned both individual and a representative ensemble of realizations
590 from two different types of anisotropic fields. Among them, we analyzed fields showing
591 preferential correlation along one planar axis, thus resembling a stream-channeled system,
592 and fields showing preferential correlation along the planar axis and the vertical direction,
593 thus resembling vertically tilted fractures.

594 Our simulations help to illustrate that β effectively displays an apparent directional
595 behavior in anisotropic formations, for both types of fields. The directionality of β is
596 remarkable, since β is usually adopted as an isotropic parameter in nonlocal formulations
597 used to fit BTCs from tracer tests in heterogeneous media. The key aspect is that β
598 behaves in a qualitatively similar manner to the anisotropic distribution of K , thus proving
599 that a link between physical (K) and mathematical (β) can be built in the limit of CFTTs
600 in anisotropic formations.

601 Our setup is far from ergodic transport and therefore unlikely to provide universally
602 exportable quantitative conclusions. Nonetheless, two main parameters seem to play a
603 major role in controlling the behavior of β :

604 • the dimensionless parameter r_λ , which expresses the ratio between travel distance
605 (radius between the injection and the extraction locations) relative to the underlying
606 correlation distances. This result is in agreement with the analysis by *Pedretti et al.* [2013],
607 who found that r_λ is a characteristic value indicating the apparent effect of stratification
608 in controlling anomalous tailing in BTCs during convergent flow tracer tests. The more
609 stratified the injection, the larger β ; as a consequence, β is maximum as $r_\lambda \rightarrow 0$ (perfectly
610 stratified transport), while β tends to a minimum value as $r_\lambda \rightarrow \infty$ (due to effects of
611 vertical mixing and plume homogenization).

612 • the dimensionless parameter L_z , which sets the relative "homogenization" during the
613 injection of the solute in the aquifer. It was found that the ensemble mean values for β
614 for fields (A) are substantially different (generally lower) from those for fields (B).

615 A more detailed analysis showed that a strong relationship may exist between β and
616 BTC peak times. This relationship is stronger for fields (A) than fields (B), which is
617 consistent with the fact that when the injected solutes are less homogenized (fields A),
618 solutes tend to be more stratified, giving rise to more transport variability between layers
619 making up the aquifer. This is consistent with the analysis of *Pedretti et al.* [2013].

620 We can conclude from our analysis that these results give new insights into understand-
621 ing how to relate upscaled parameters to physical soil parameters, which is a critical step
622 to understanding how to adequately use these effective solutions for predictive purposes.
623 In this type of setting, connectivity and stratification, which are intimately related, seem
624 to determine how likely the system tends to behave as an apparent single- or multi-porosity
625 domain. From a practical perspective, the directional behavior of β in anisotropic set-
626 tings provides empirical evidence of physical constraints to one of the parameters used

627 in multi-rate mass transfer models, which to date have not been proven to be predictive
628 under advection-dominated transport conditions.

Acknowledgments

629 DP acknowledges the funding provided by the Spanish Ministry of Education through
630 the FPU-Med Scholarship program. XS acknowledges Program ICREA Academia. Ad-
631 ditional funding was provided by the Spanish Ministry of Science and Innovation, via
632 projects Consolider-Ingenio 2010 (CSD2009-00065) and FEAR (CGL2012-38120). DB
633 was in part supported by the National Science Foundation under Grant No. EAR-1113704

References

- 634 Aris, R. (1956), On the dispersion of a solute by diffusion, convection and exchange between
635 phases, *Proc R Soc Lond*, *252*(1271), 538–550, doi:10.1098/rspa.1959.0171.
- 636 Becker, M., and A. M. Shapiro (2000), Tracer transport in fractured crystalline rock: Evidence
637 of nondiffusive breakthrough tailing, *Water Resour. Res.*, *36*, 1677–1686.
- 638 Benson, D. A., and M. M. Meerschaert (2009), A simple and efficient random walk solution
639 of multi-rate mobile/immobile mass transport equations, *Advances in Water Resources*, *32*,
640 532–539, doi:10.1016/j.advwatres.2009.01.002.
- 641 Bolster, D., M. Barahona-Palomo, M. Dentz, D. F. Garcia, X. Sanchez-Vila, P. Trinchero, C. Val-
642 hondo, and D. M. Tartakovsky (2009), Probabilistic risk assessment applied to contamination
643 scenarios in porous media, *Water Resour. Res.*, *45*, W06,413, doi:10.1029/2008WR007551.
- 644 Cameron, D. R., and A. Klute (1997), Convective-dispersive solute transport with a combined
645 equilibrium and kinetic adsorption model, *Water Resources Research*, *13*(1), 183–188, doi:
646 10.1029/WR013i001p00183.
- 647 Carrera, J., X. Sanchez-Vila, I. Benet, A. Medina, G. Galarza, and J. Guimerà (1998), On matrix
648 diffusion: formulations, solution methods and qualitative effects., *Hydrogeol. J.*, *6*, 178–190,
649 doi:10.1007/s100400050143.
- 650 Clauset, A., C. R. Shalizi, and M. E. Newman (2007), Power-law distribution in empirical data,
651 *SIAM Review*, *51*, 661–703, doi:10.1137/070710111.
- 652 Dagan, G. (1989), *Flow and Transport in Porous Formations*, Springer-Verlag, Berlin.
- 653 de Barros, F. P., D. Bolster, X. Sanchez-Vila, and W. Nowak (2011), A divide and conquer
654 approach to cope with uncertainty, human health risk, and decision making in contaminant
655 hydrology, *Water Resources Research*, *47*(5).

- 656 Donado, L. D., X. Sanchez-Vila, M. Dentz, J. Carrera, and D. Bolster (2009), Multicomponent
657 reactive transport in multicontinuum media, *Water Resources Research*, 45(11).
- 658 Fernàndez-Garcia, D., X. Sanchez-Vila, and T. H. Illangasekare (2002), Convergent-flow tracer
659 tests in heterogeneous media: combined experimental-numerical analysis for determination
660 of equivalent transport parameters, *Journal of Contaminant Hydrology*, 57(1-2), 129 – 145,
661 doi:10.1016/S0169-7722(01)00214-5.
- 662 Fernàndez-Garcia, D., T. H. Illangasekare, and H. Rajaram (2004), Conservative and sorptive
663 forced-gradient and uniform flow tracer tests in a three-dimensional laboratory test aquifer,
664 *Water Resources Research*, 40, W10,103, doi:10.1029/2004WR003112.
- 665 Fernàndez-Garcia, D., H. Rajaram, and T. H. Illangasekare (2005), Assessment of the predic-
666 tive capabilities of stochastic theories in a three-dimensional laboratory test aquifer: Effective
667 hydraulic conductivity and temporal moments of breakthrough curves, *Water Resources Re-*
668 *search*, 41, W04,002, doi:10.1029/2004WR003523.
- 669 Fiori, A., I. Jankovic, and G. Dagan (2006), Modeling flow and transport in highly heterogeneous
670 three-dimensional aquifers: Ergodicity, gaussianity, and anomalous behavior-2. approximate
671 semianalytical solution, *Water Resources Research*, 42, W06D13, doi:10.1029/2005WR004752.
- 672 Flach, G. (2012), Relationship between dual-domain parameters and practical characterization
673 data, *Ground Water*, 50(2), 216–229.
- 674 Gelhar, L. W. (1993), *Stochastic subsurface hydrology*, Prentice Hall, NJ.
- 675 Gelhar, L. W., and C. L. Axness (1983), Three-dimensional stochastic analysis of macrodispersion
676 in aquifers, *Water Resources Research*, 19(1), 161, doi:10.1029/WR019i001p00161.
- 677 Gelhar, L. W., A. L. Gutjahr, and R. L. Naff (1979), Stochastic analysis of macrodispersion in a
678 stratified aquifer, *Water Resources Research*, 15(6), 1387–1397.

- 679 Goltz, M. N., and P. V. Roberts (1987), Using the method of moments to analyze three-
680 dimensional diffusion-limited solute transport from temporal and spatial perspectives, *Water*
681 *Resources Research*, *23*(8), 1575–1585, doi:10.1029/WR023i008p01575.
- 682 Gouze, P., Y. Melean, T. Le Borgne, M. Dentz, and J. Carrera (2008), Non-fickian dispersion
683 in porous media explained by heterogeneous microscale matrix diffusion, *Water Resources*
684 *Research*, *44*, W11,416, doi:10.1029/2007WR006690.
- 685 Guswa, A. J., and D. L. Freyberg (2002), On using the equivalent conductivity to characterize
686 solute spreading in environments with low-permeability lenses, *Water Resources Research*,
687 *38*(8), 7-1–7-14, doi:10.1029/2001WR000528.
- 688 Haggerty, R., and S. Gorelick (1995), Multiple-rate mass transfer for modeling diffusion and
689 surface reactions in media with pore-scale heterogeneity, *Water Resour. Res.*, *31*(10), 2383–
690 2400, doi:10.1029/95WR10583.
- 691 Haggerty, R., and P. C. Reeves (2002), Stammt-1 1.0, formulation and user’s guide, technical
692 report erms 520308, *Tech. rep.*, Sandia National Laboratories, Albuquerque, NM, USA.
- 693 Haggerty, R., S. A. McKenna, and L. C. Meigs (2000), On the late-time behavior of tracer test
694 breakthrough curves, *Water Resour. Res.*, *36*(12), 3467–3479, doi:10.1029/2000WR900214.
- 695 Harvey, C. F., and S. Gorelick (1995), Temporal moment-generating equations: Modeling trans-
696 port and mass transfer in heterogeneous aquifers, *Water Resources Research*, *31*(8), 1895–1911,
697 doi:10.1029/95WR01231.
- 698 Knudby, C., and J. Carrera (2006), On the relationship between indicators of geostatistical,
699 flow and transport connectivity, *Advances in Water Resources*, *28*(4), 405 – 421, doi:DOI:
700 10.1016/j.advwatres.2004.09.001.

- 701 Koltermann, C. E., and S. Gorelick (1996), Heterogeneity in sedimentary deposits: A review of
702 structure-imitating, process-imitating, and descriptive approaches, *Water Resources Research*,
703 *32*(9), 2617–2658.
- 704 Le Borgne, T., M. Dentz, and J. Carrera (2008), Lagrangian statistical model for transport in
705 highly heterogeneous velocity fields, *Physical Review Letters*, *101*, 090,601.
- 706 Matheron, G. (1967), *Elements Pour Une Theorie des Milieux Poreux*, Masson et Cie, Paris.
- 707 Moench, A. (1989), Convergent Radial Dispersion: A Laplace Transform Solution for Aquifer
708 Tracer Testing, *Water Resour. Res.*, *25*(3), 439–447, doi:10.1029/WR025i003p00439.
- 709 Neuman, S. P., and D. M. Tartakovsky (2009), Perspective on theories of non-fickian transport in
710 heterogeneous media, *Advances in Water Resources*, *32*, 670–680.
- 711 Nkedi-Kizza, P., J. W. Biggar, H. M. Selim, M. T. Van Genuchten, P. J. Wierenga, J. M.
712 Davidson, and D. R. Nielsen (1984), On the equivalence of two conceptual models for describing
713 ion exchange during transport through an aggregated oxisol, *Water Resources Research*, *20*(8),
714 1123, doi:10.1029/WR020i008p01123.
- 715 Parker, J. C., and M. T. Van Genuchten (1984), Flux-averaged and volume-averaged concentra-
716 tions in continuum approaches to solute transport, *Water Resources Research*, *20*(7), 866–872.
- 717 Pedretti, D., and D. Fernández-García (2013), A locally-adaptive and automatic method to
718 estimate heavily-tailed breakthrough curves from particle distributions, *Advances in Water*
719 *Resources*, *59*, 52–65, doi:10.1016/j.advwatres.2013.05.006.
- 720 Pedretti, D., and A. Fiori (2013), Travel times distribution under convergent radial flow in het-
721 erogeneous formations: insight from an exact stratified model, *Advances in Water Resources*,
722 doi:10.1016/j.advwatres.2013.07.013.

- 723 Pedretti, D., D. Fernàndez-Garcia, D. Bolster, and X. Sanchez-Vila (2013), On the formation
724 of heavy-tailed breakthrough curves during convergent flow tracer tests in three-dimensional
725 heterogeneous sandy aquifers, *Water Resources Research*, doi:10.1002/wrcr.20330.
- 726 Ptak, T., M. Piepenbrink, and E. Martac (2004), Tracer tests for the investigation of heteroge-
727 neous porous media and stochastic modelling of flow and transport - a review of some recent
728 developments, *Journal of Hydrology*, 294, 122–163.
- 729 Renard, P., and D. Allard (2013), Connectivity metrics for subsurface flow and transport, *Ad-
730 vances in Water Resources*, 51, 168–196, doi:10.1016/j.advwatres.2011.12.001.
- 731 Riva, M., A. Guadagnini, D. Fernandez-Garcia, X. Sanchez-Vila, and T. Ptak (2008), Rela-
732 tive importance of geostatistical and transport models in describing heavily tailed break-
733 through curves at the Lauswiesen site, *Journal of Contaminant Hydrology*, 101, 1–13, doi:
734 10.1016/j.jconhyd.2008.07.004.
- 735 Rubin, Y. (2003), *Applied stochastic hydrogeology*, Oxford University Press, USA.
- 736 Rubin, Y., M. A. Cushey, and A. Wilson (1997), The moments of the breakthrough curves of
737 instantaneously and kinetically sorbing solutes in heterogeneous geologic media: Prediction and
738 parameter inference from field measurements, *Water Resources Research*, 33(11), 2465–2481,
739 doi:10.1029/97WR01229.
- 740 Salamon, P., D. Fernàndez-Garcia, and J. Gomez-Hernandez (2007), Modeling tracer transport
741 at the made site: The importance of heterogeneity, *Water Resources Research*, 43, W08,404,
742 doi:10.1029/2006WR005522.
- 743 Sanchez-Vila, X., and J. Carrera (1997), Directional effects on convergent flow tracer tests,
744 *Mathematical Geology*, 29(4), 551–569, doi:10.1007/BF02775086.

- 745 Sanchez-Vila, X., J. Carrera, and J. Girardi (1996), Scale effects in transmissivity, *Journal of*
746 *Hydrology*, 183(1-2), 1–22.
- 747 Sharifi Haddad, A. , H. Hassanzadehm, and J. Abedi (2012), Advective–diffusive mass trans-
748 fer in fractured porous media with variable rock matrix block size. *Journal of Contaminant*
749 *Hydrology*, 113, 94–107, doi:10.1016/j.jconhyd.2012.02.008
- 750 Silva, O., J. Carrera, M. Dentz, S. Kumar, A. Alcolea, and M. Willmann (2009), A general real-
751 time formulation for multi-rate mass transfer problems, *Hydrol. Earth Syst. Sci.*, 13, 1399–1411,
752 doi:10.5194/hess-13-1399-2009.
- 753 Trinchero, P., X. Sanchez-Vila, and D. Fernàndez-Garcia (2008), Point-to-point connectivity, an
754 abstract concept or a key issue for risk assessment studies?, *Advances in Water Resources*,
755 31(12), 1742–1753, doi:10.1016/j.advwatres.2008.09.001.
- 756 Valocchi, A. J. (1985), Validity of the local equilibrium assumption for modeling sorbing solute
757 transport through homogeneous soils, *Water Resources Research*, 21(6), 808.
- 758 Willmann, M., J. Carrera, and X. Sanchez-Vila (2008), Transport upscaling in heterogeneous
759 aquifers: What physical parameters control memory functions?, *Water Resour. Res.*, 44,
760 W12,437, doi:10.1029/2007WR006531.
- 761 Willmann, M., J. Carrera, X. Sanchez-Vila, O. Silva, and M. Dentz (2010), Coupling of mass
762 transfer and reactive transport for nonlinear reactions in heterogeneous media, *Water Resources*
763 *Research*, 46(7).
- 764 Zhang, Y., D. A. Benson, and B. Baeumer (2007), Predicting the tails of breakthrough
765 curves in regional-scale alluvial systems, *Ground Water*, 45(4), 473–484, doi:10.1111/j.1745-
766 6584.2007.00320.x.

767 Zinn, B., and C. F. Harvey (2003), When good statistical models of aquifer heterogene-
768 ity go bad: A comparison of flow, dispersion and mass transfer in connected and multi-
769 variate gaussian hydraulic conductivity fields, *Water Resources Research*, *39*(3), 1051, doi:
770 10.1029/2001WR001146.

771 Zinn, B., L. C. Meigs, C. F. Harvey, R. Haggerty, W. J. Peplinski, and C. Freiherr von Schwerin
772 (2004), Experimental Visualization of Solute Transport and Mass Transfer Processes in Two-
773 Dimensional Conductivity Fields with Connected Regions of High Conductivity, *Environmental*
774 *Science & Technology*, *38*(14), 3916-3926, doi:10.1021/es034958g.

Appendix A: Derivation of (5)

Benson and Meerschaert [2009] show that the continuum MRMT equation is equivalent to a two-state Markov chain model wherein a particle transfers between mobile and immobile states. They show that a particle has exponentially distributed mobile times M_i (with mean $1/\beta\lambda$), and random times in the immobile phase W_i with mean waiting time (if it is well-defined) of $1/\lambda$. This defines β in this model as the ratio of mean times in the immobile and mobile zones ($\frac{1}{\lambda}/\frac{1}{\beta\lambda} = \beta$). We may define the first arrivals as those particles that spend little or no time in the immobile phase with arrival time $\sum M_i$ and those particles that spend ample time in the immobile zone on their journey as having mean arrival time $\sum M_i + W_i$. Taking expectations and the ratio, and eliminating the sum (which is an identical number for each):

$$\frac{\sum E[M_i] + E[W_i]}{\sum E[M_i]} = \frac{1/\beta\lambda + 1/\lambda}{1/\beta\lambda} = 1 + \beta = \frac{\mu_t^1}{t_{MT}} \quad (\text{A1})$$

775 On the far right hand side we recognize that the mean arrival time is the sum of the mean mobile
 776 and mean immobile times. Note that β is independent of any mass-transfer rate distribution or
 777 memory functions.

Figure 1. Three different anisotropic geological environments: (A) two conceptual sketches of a fluvial sedimentation processes depending on the nature of the river (braided or meander) (from *Koltermann and Gorelick* [1996]); (B) an outcrop of a formation in Southern Spain, showing subvertical fracturing and the potential of an axisymmetric anisotropy with a horizontal axis; (C) The Grand Canyon in the US, characteristic of axisymmetric anisotropy with vertical axis.

Figure 2. Example of simulations of different architecture of random hydraulic conductivity fields (A) and (B), reproducing the corresponding geological setups in Fig. 1. I indicates integral scales, and e anisotropy ratios of the integral scales. W marks the location of the fully penetrating pumping well, and R_i, U_i the different injection locations ($i=1,\dots,4$).

Figure 3. Map representing the logarithm (base 10) of the capacity coefficient (β), for fields (A) (left) and (B) (right); at each point the $\log(\beta)$ value is estimated from the BTC recorded from a tracer injected at that particular location.

Figure 4. Ensemble of 1000 estimated density functions obtained after injecting particles at two different locations, R4 (right plots) and U4 (left plots) in fields (A) (top) and fields (B) (bottom). All plots show the same axis lengths to emphasise the different shape depending on the field and the injection locations. Time t_c is dimensionless (see text). Colored curves correspond to individual selected realizations and are only highlighted to show different shapes.

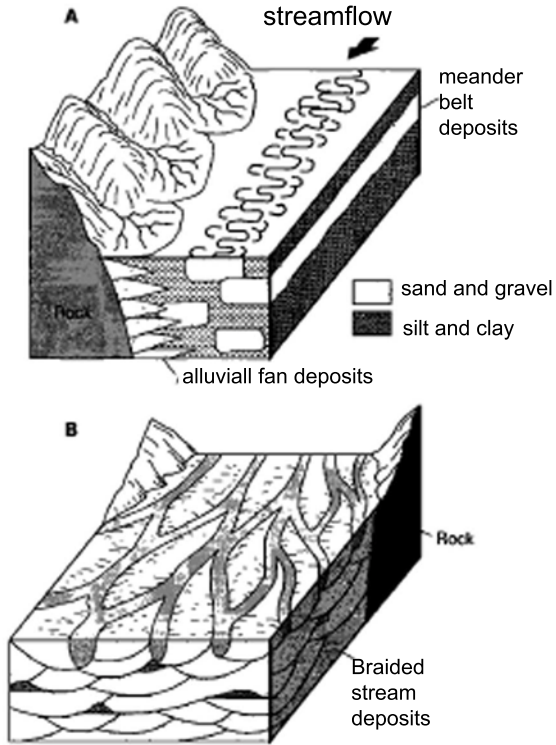
Figure 5. Correlation between β , t_m and μ_t^1 at locations R4 and U4 (all simulations for fields (A) are plotted). The red line represents the best-fitting curve for each case. RMSE= root mean square error, R^2 = Pearson coefficient.

Figure 6. Correlation between β , t_m and μ_t^1 at locations R4 and U4 (all simulations for fields (B) are plotted). The red line represents the best-fitting curve for each case. RMSE= root mean square error, R^2 = Pearson coefficient.

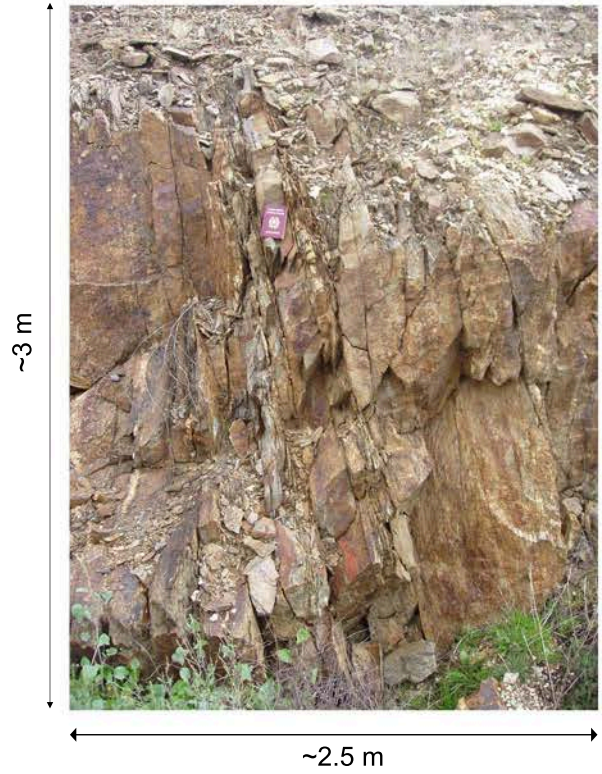
Figure 7. Visual relationship between anisotropic structure, connectivity and mass-transfer capacity coefficient for one individual realization of fields (A). Maps reproduce (1) the vertically-integrated log-transformed hydraulic conductivity; (2) the capacity coefficient β (in \log_{10}); (3) the BTC peak time t_m (or the map of connectivity - inversely proportional to t_m), and (4) the advection time μ_t^1 . 'W' indicates the position of the well. The ellipse highlights the most connected channel in map (3) with correspondingly large $\log(\beta)$ found in map (2) (see discussion in the text).

Figure 8. Correlation between β , t_m and μ_t^1 for the individual realization analysis (all injection points are plotted). The red line represents the best-fitting curve for each case. RMSE= root mean square error, R^2 = Pearson coefficient.

(A) : coarser-grain sediments oriented preferentially along the y-axis



(B) : fractures oriented preferentially along the yz-plane

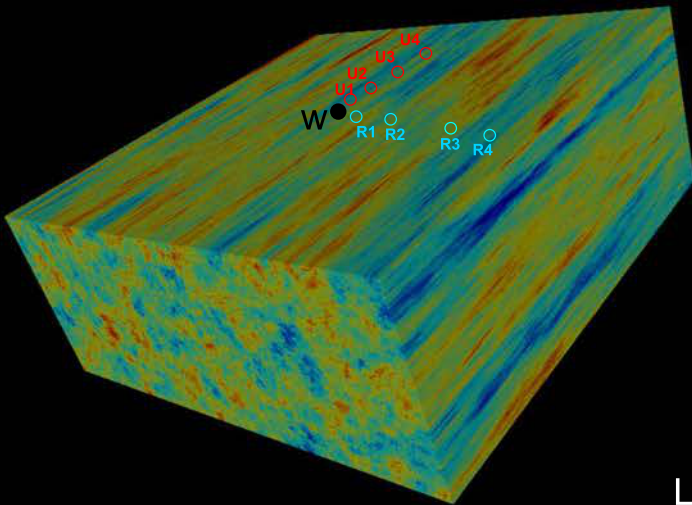


(C) : stratified medium with beds parallel to xy plane



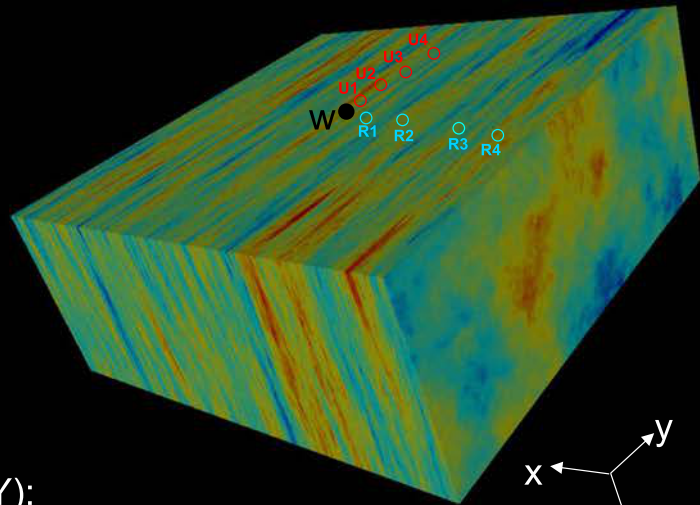
Field (A) $I_x=4, I_y=40, I_z=4$

$e_{xy}=0.1, e_{yz}=10, e_{xz}=1$

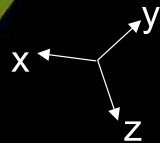
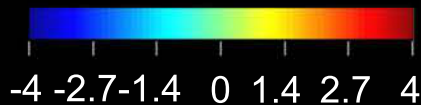


Field (B) $I_x=4, I_y=40, I_z=40$

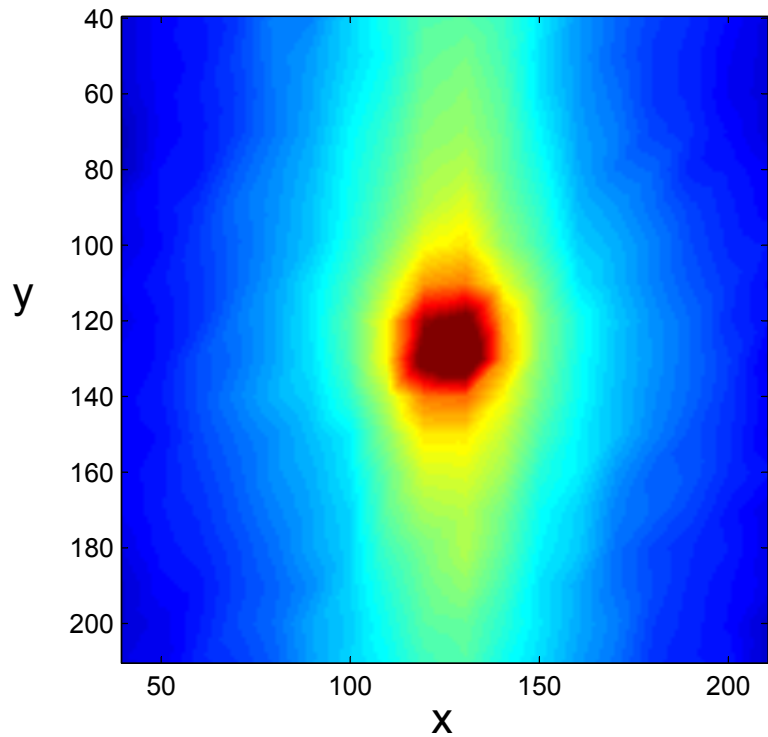
$e_{xy}=0.1, e_{yz}=1, e_{xz}=0.1$



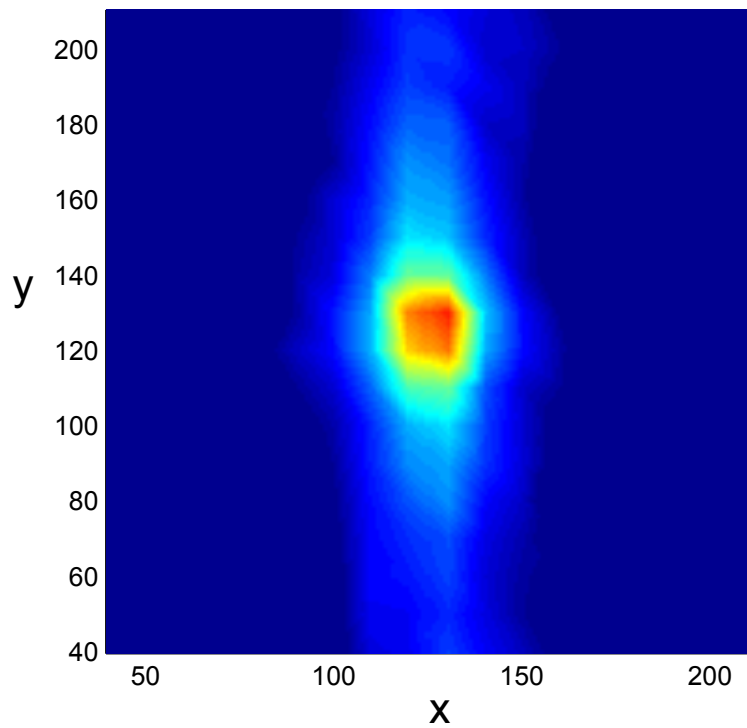
Legend (Y):



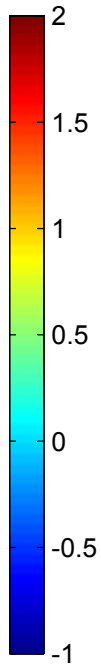
Field (A) ($I_y=40, I_x=I_z=4$)

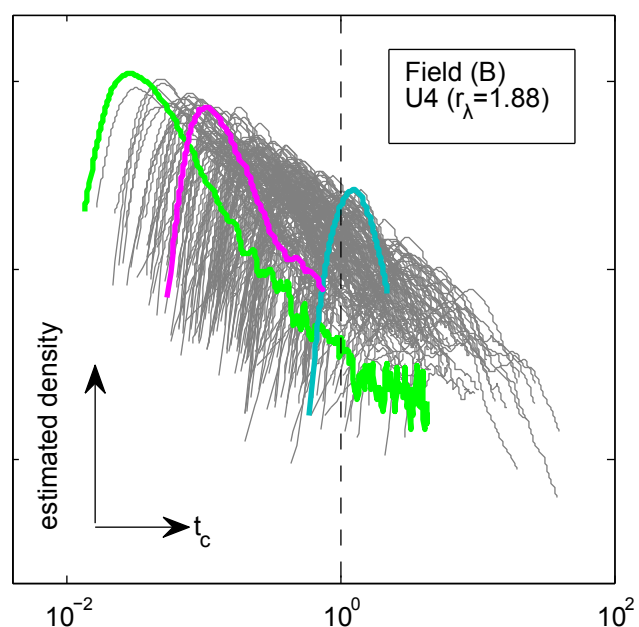
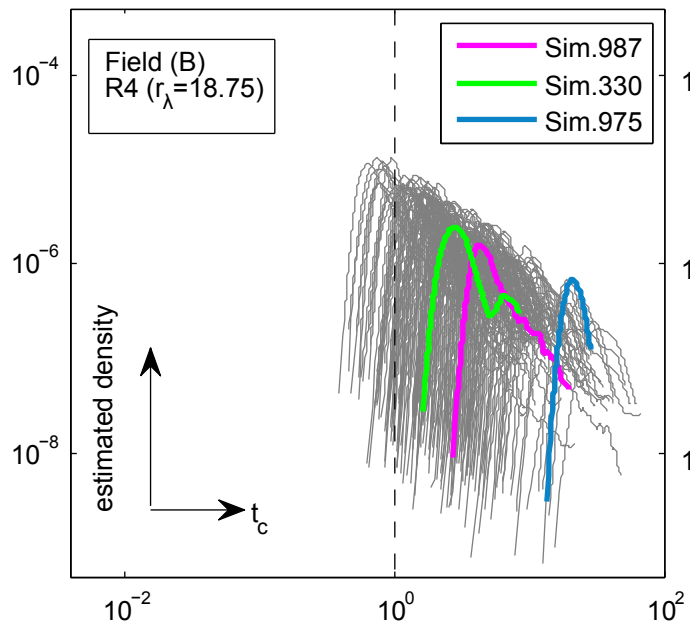
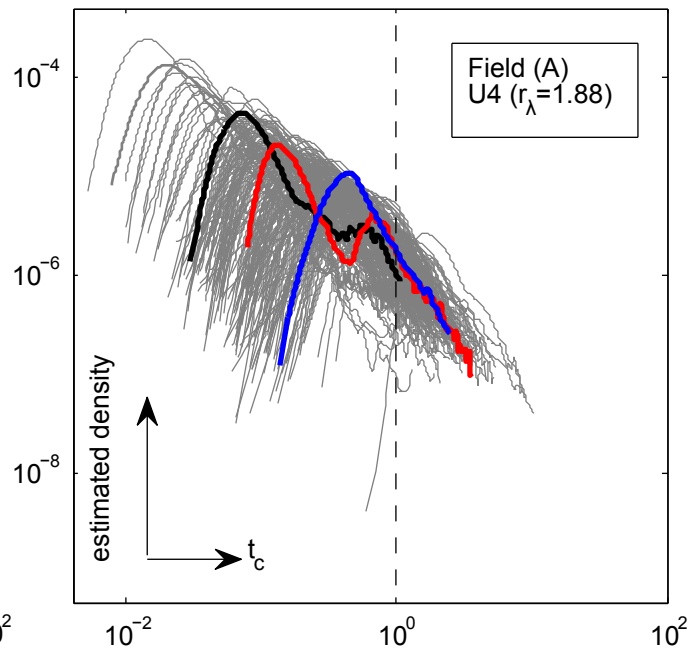
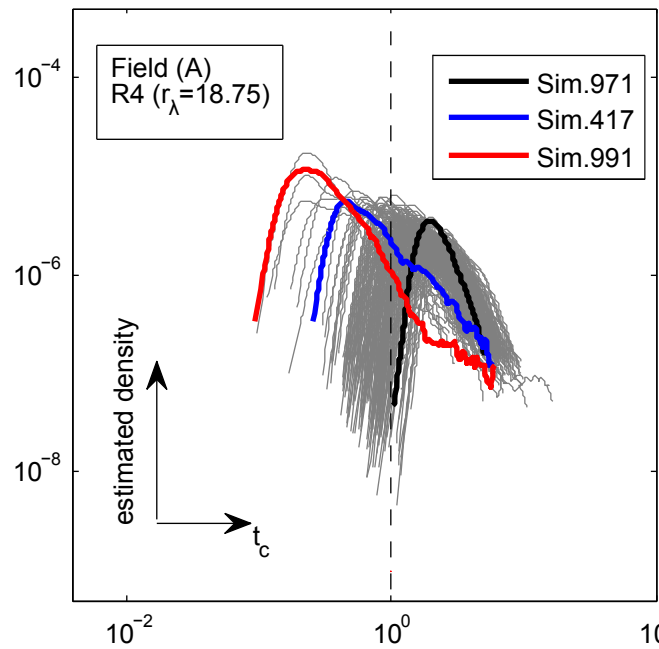


Field (B) ($I_y, I_z=40, I_x=4$)



$\log(\beta)$

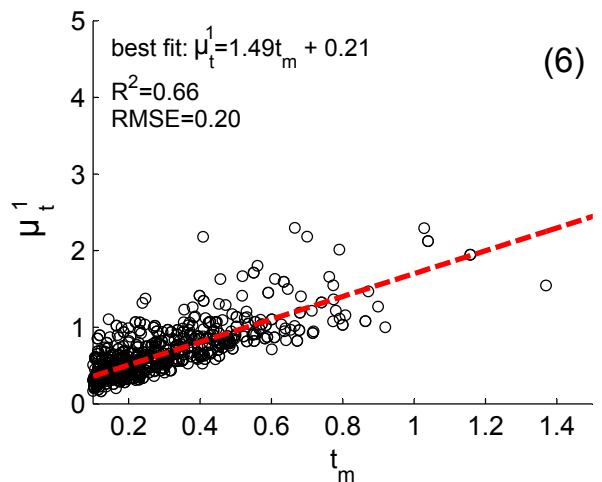
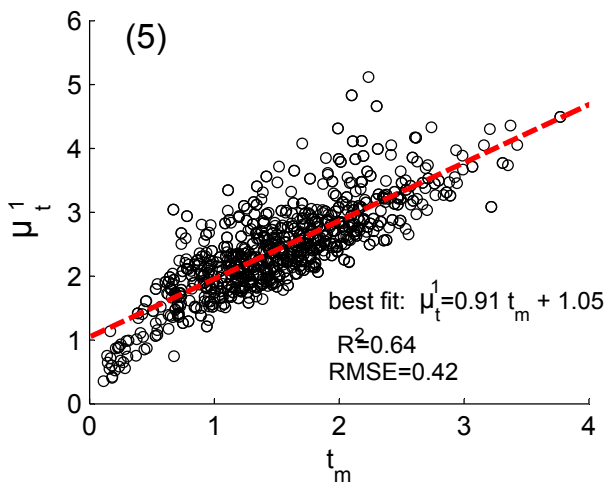
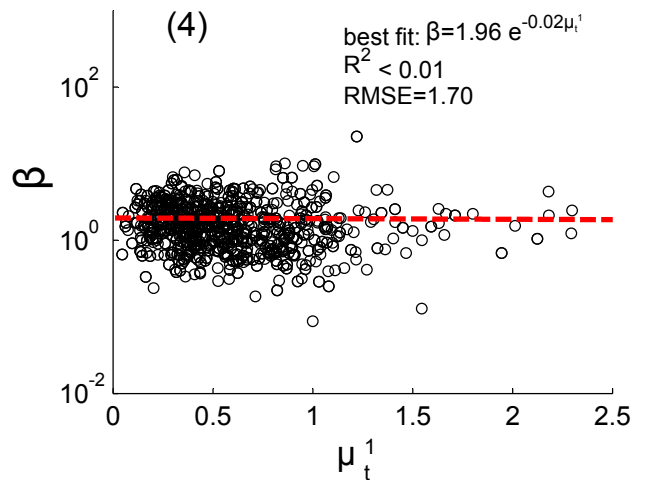
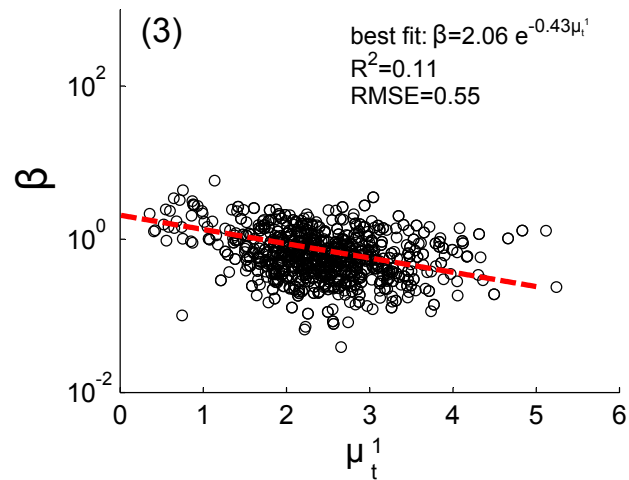
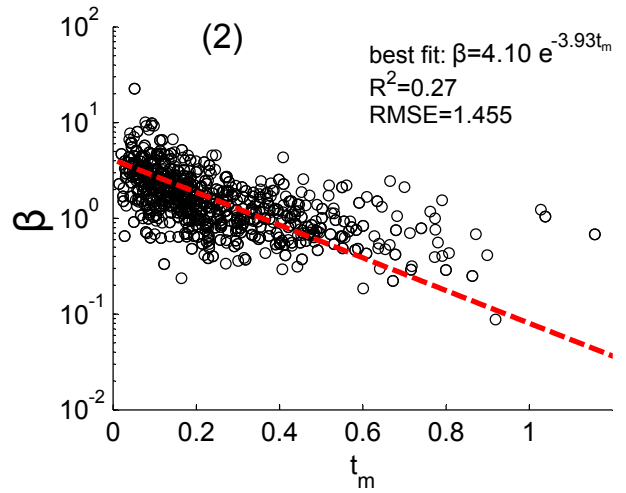
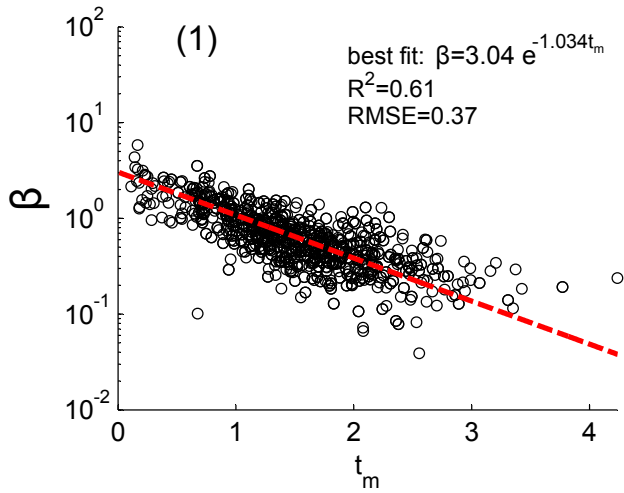




Field type A ($b/l_z=25$)

Injection at R4 (orthogonal to main anisotropy axis - $r = 18.75$)

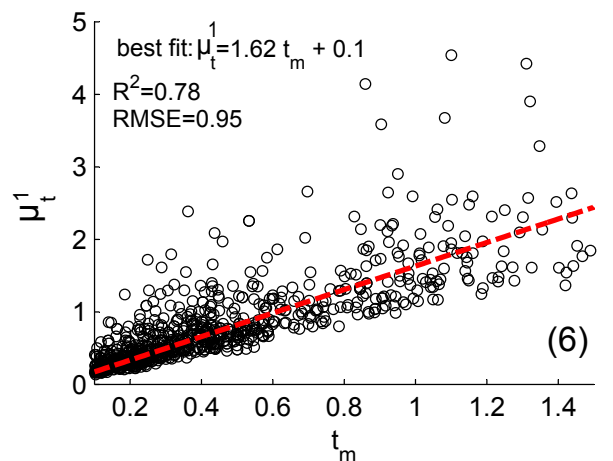
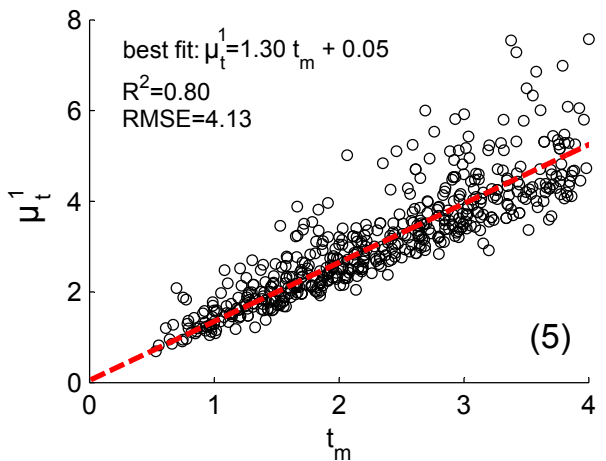
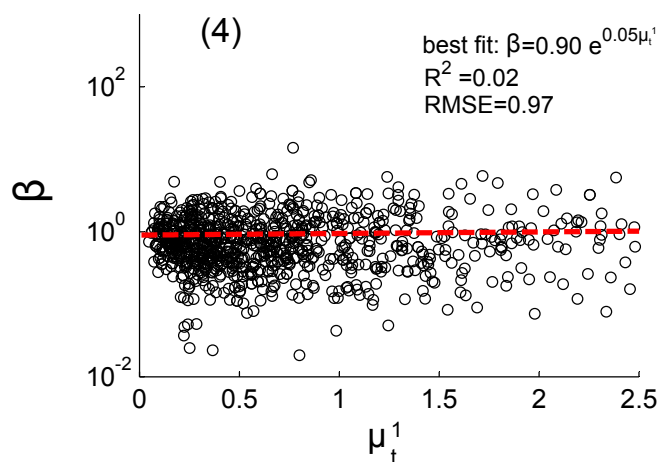
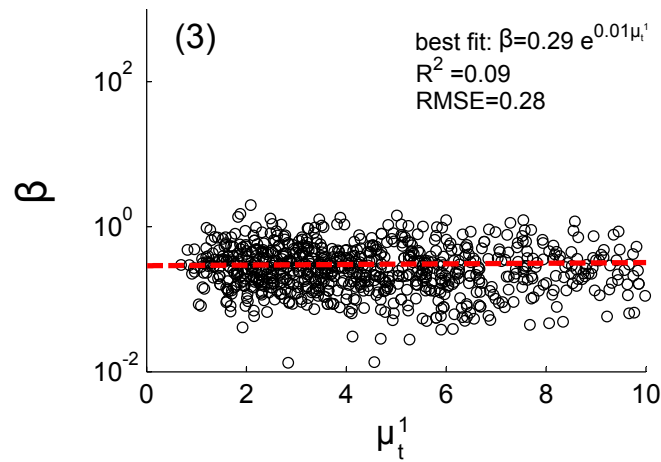
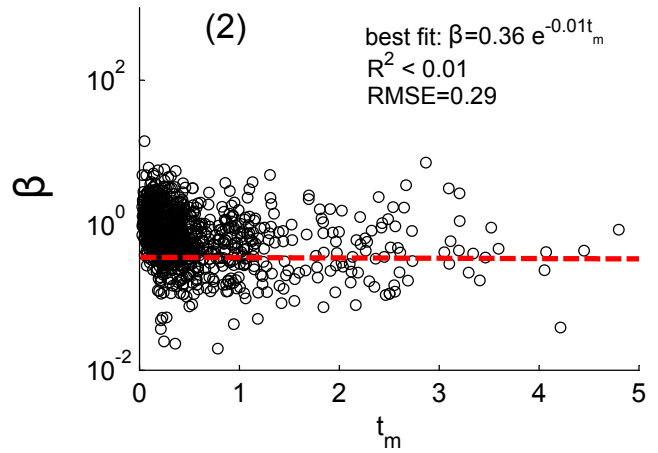
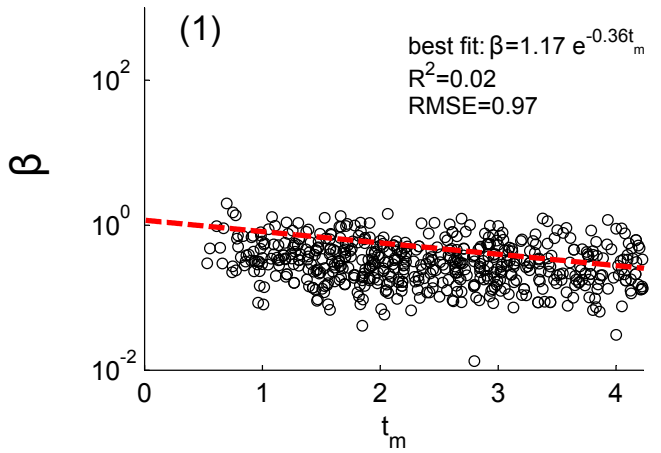
Injection at U4 (collinear with main anisotropy axis $r = 1.88$)



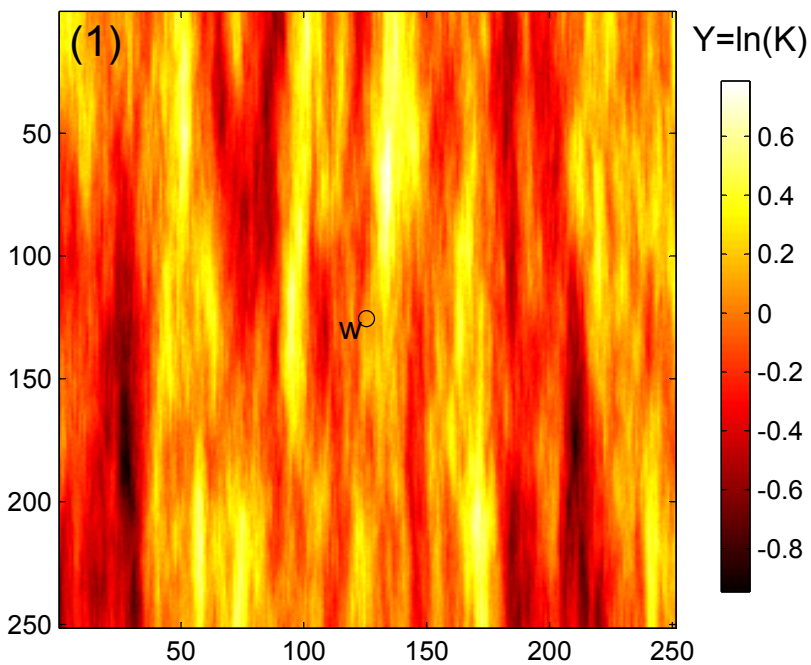
Field type B ($b/l_z = 2.5$)

Injection at R4 (orthogonal to main anisotropy axis - $r = 18.75$)

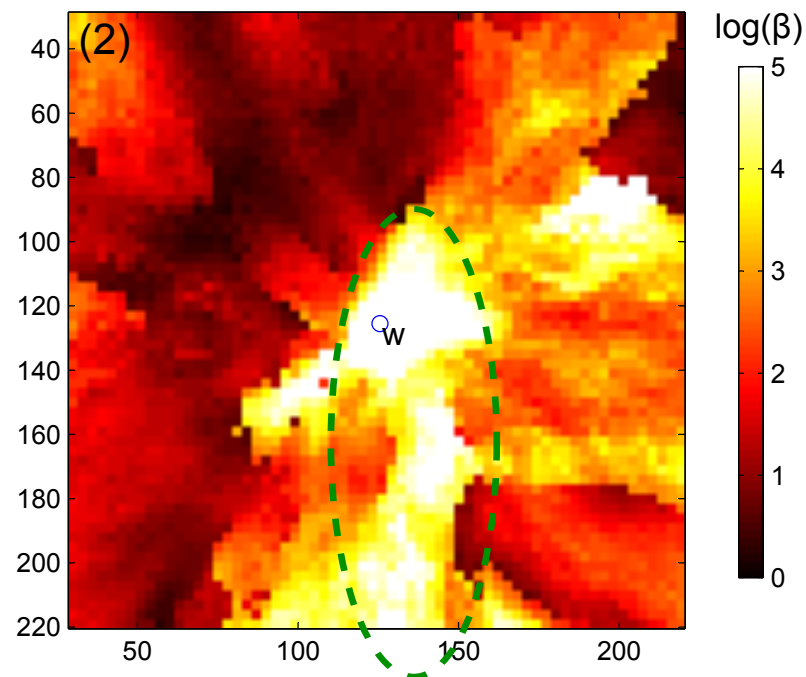
Injection at U4 (collinear with main anisotropy axis $r = 1.88$)



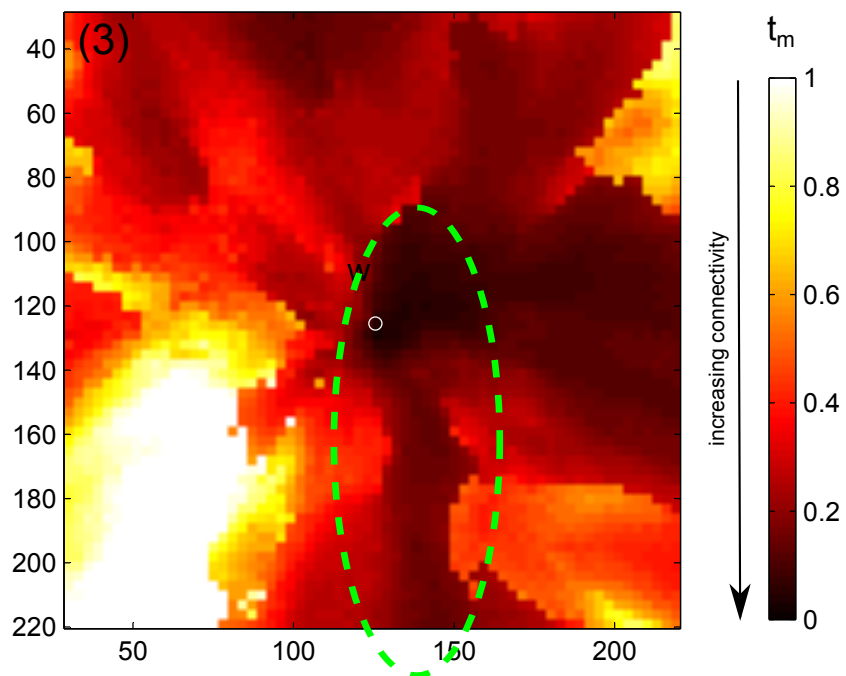
Vertically integrated Y-field



Estimated capacity coefficient



BTC peak time (transport connectivity)



Travel time first moment

